Electron-ion thermal equilibration dynamics in femtosecond heated warm dense copper

N. Jourdain,[1,2] L. Lecherbourg,[2] V. Recoules,[2] P. Renaudin,[2] and F. Dorchies[1,*]
[1]*Université de Bordeaux, CNRS, CEA, CELIA (Centre Lasers Intenses et Applications), UMR 5107, F-33400 Talence, France*
[2]*CEA-DAM-DIF, F-91297 Arpajon, France*

(Received 22 December 2017; published 26 February 2018)

Nonequilibrium warm dense copper produced by a femtosecond optical laser pulse is investigated with x-ray absorption near-edge spectroscopy. A laser-plasma-based tabletop device is set up to probe a pre-edge structure observed near the L edge with a picosecond resolution. Careful *ab initio* calculations are used to retrieve the electron temperature evolution up to equilibration with ions. Measurements are well reproduced by two-temperature model calculations based on temperature-dependent parameters, provided that the hydrodynamic expansion is taken into account. At the highest temperatures investigated (∼20 000 K), the last affects significantly the energy balance between electrons and ions.

DOI: 10.1103/PhysRevB.97.075148

I. INTRODUCTION

The warm dense matter (WDM) regime falls in between solid condensed matter and hot plasma. The prediction of physical properties constitutes a major challenge to modern science, as it requires the description of both strongly correlated ions and degenerated electrons, as well as an understanding of their interplay [1]. Investigations are driven by great interest in high-pressure science, astrophysics and planetology [2–4], inertial confinement fusion [5,6], and laser processes [7].

WDM can be transiently reached in the laboratory by irradiating a foil with an ultrashort light pulse, in either the optical [8–16], xuv [17,18], or x-ray range [19,20] (or, alternatively, with ions [21,22]). In all these, the electrons are initially excited while the ions remain cold. This results in a nonequilibrium situation before electrons and ions relax to reach a thermal equilibrium in a few picoseconds. In the past few years, several experiments aimed at studying the nonequilibrium physics driven by a femtosecond laser pulse thanks to the development of different time-resolved techniques, ranging from femtosecond optical probing [8–10,14] to femtosecond x-ray and electron diffraction [11,23,24] and picosecond x-ray absorption spectroscopy [12,13,15,16]. Among other diagnostics, x-ray absorption near-edge spectroscopy (XANES) is a powerful tool for studying nonequilibrium physics in warm dense matter since it gives information on both the electronic structure and the local atomic order, which could highlight their dynamic interplay [25].

The two-temperature model (TTM) was considered early on to address the nonequilibrium physics, reducing the system to two subpopulations (electrons and ions) characterized by their respective temperature [26]. Within this representation, the energy transfer from electrons to ions is described with only a few parameters, such as electron and ion heat capacities C_e and C_i, and the electron-ion coupling parameter G. Near ambient conditions, free-electron gas models (FEG) lead to satisfactory values of these coefficients. They have to be reevaluated at the high temperatures encountered in WDM. Lin *et al.* have proposed a dependence on the electron temperature for C_e and G for various metals [27]. They regarded electrons as a high-temperature Fermi distribution, and the electron and phonon densities of states (DOSs) were fixed to those of the cold solid. Such strong assumptions need to be studied in detail, especially concerning the relatively long electron-ion thermal equilibration. Indeed, the DOSs are expected to be significantly modified when the solid turns to disordered WDM. Cho *et al.* first proposed time-resolved XANES on a synchrotron beamline to retrieve the temporal behavior of electron temperature T_e in warm dense copper [12]. More recently, they suggested that the electron heat capacity C_e and the electron-ion coupling parameter G could be directly inferred [16] under the assumption of a constant solid density.

In this paper, we revisit the study of nonequilibrium warm dense copper by performing time-resolved XANES (TR-XANES) measurements near the L edge on a tabletop setup. The picosecond x-ray source duration allows us to resolve the electron-ion thermal equilibration dynamics in a range of temperature up to ∼20 000 K. Careful *ab initio* calculations are used to retrieve the electron temperature without ambiguity from the pre-edge structure that is observed near the $L3$ edge. Data are compared with in-depth hydrodynamic two-temperature calculations forced by laser energy deposition measurements. Good agreement is observed when considering the temperature-dependent parameters from Lin *et al.* [27], provided that the hydrodynamic expansion is taken into account. Indeed, the latter affects significantly the energy balance between electrons and ions and hinders the straightforward determination of C_e and G that also depend on density.

II. EXPERIMENTAL METHOD

A. Laser-plasma-based tabletop setup

The experiment has been performed on the TR-XANES tabletop station developed at CELIA laboratory, which is fully described in Ref. [28]. A schematic view is shown in Fig. 1. The laser-plasma x-ray source has been adjusted in order to get a broadband optimized x-ray emission in the spectral range (0.9–1 keV) that surrounds the Cu L edges (at 0.9325 and

*fabien.dorchies@u-bordeaux.fr

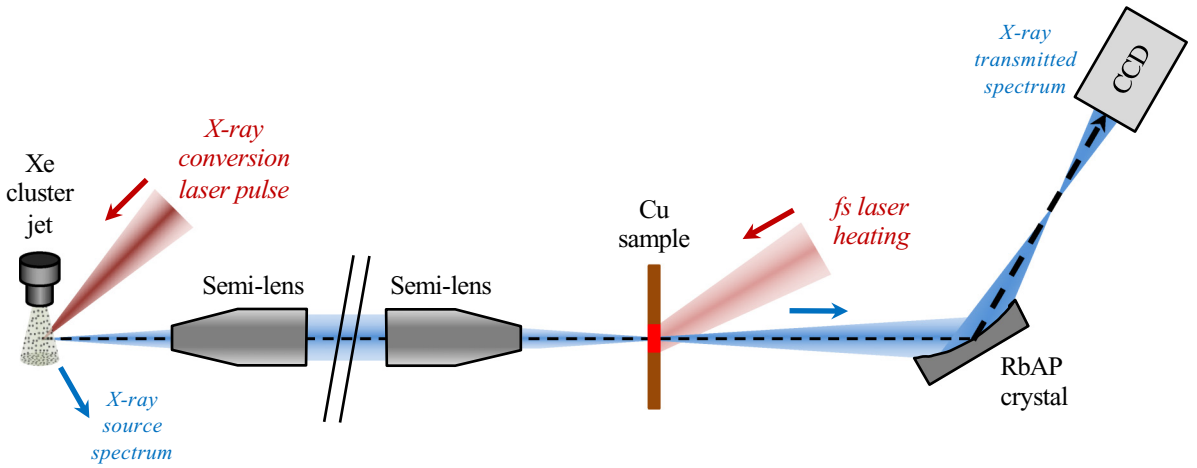

FIG. 1. Schematic view of the experimental setup. More details can be found in Ref. [28].

0.9523 keV for $L3$ and $L2$, respectively). It results from the interaction of an 80-mJ, 600-fs optical laser pulse (at 800-nm central wavelength) focused in a Xe cluster jet produced at the outlet of a supersonic nozzle 1.5 mm from the exit (backing pressure 20 bars at ambient temperature).

The x-ray source is roughly isotropic. Its spectrum is controlled on the first spectrometer. A fraction of the emission is collected in a polycapillary optics (with a semilens geometry), then transported up to another one that concentrates it on a 300-μm FWHM diameter spot in the sample plane. The transmitted spectrum is recorded on a spectrometer identical to the first one. They are both based on a cylindrical rubidium biphthalate (RbAP) crystal ($2d = 26.121$ Å) coupled to an x-ray CCD camera located in the Rowland circle in order to achieve the best spectral resolution (0.9 eV measured and limited by the crystal).

From the Xe cluster x-ray source, about 50 photons shot^{-1} eV^{-1} are registered on the transmission spectrometer near the Cu L edge. Considering the transmission of the 0.9-μm Be filter placed in front of the x-ray CCD camera, the crystal-integrated reflectivity of 3.5×10^{-4} rad, and the focusing angle of the second polycapillary, we find that 35 000 photons shot^{-1} eV^{-1} are focused on the sample.

Samples are made of an (80 ± 10)-nm copper foil deposited on a 4-μm plastic substrate and coated on the other side with 10 nm of amorphous carbon (a-C). They were heated at 30° incidence by 300-fs FWHM laser pulses with central wavelength $\lambda = 800$ nm coming from the same laser system, then naturally synchronized with the x-ray source. A flat-top transverse profile is produced on the sample plane within an ∼1-mm-diameter spot. Its position and size are shot-to-shot controlled with an imaging diagnostic of the reflected beam (not shown in Fig. 1). A maximum transverse displacement of ±60 μm has been observed over the entire experiment. In view of the x-ray spot size, that guarantees that the probed areas are always uniformly heated. The laser energy is varied in order to adjust the incident fluence on the sample.

B. Experimental procedure

With the laser fluences under consideration being well above the ablation threshold, the sample needs to be moved to present a fresh surface shot after shot. More than 1000 shots are achievable on a single sample. The procedure detailed in Ref. [29] is applied to get the absorption spectra from the raw spectrometer measurements. Essentially, a normalization with the first spectrometer is used to prevent residual fluctuations of the x-ray source. And a preliminary set of measurements is performed without any sample in order to get rid of the systematic defects of the crystals. Three series are then registered through samples: (i) a cold sample (heating beam off), (ii) a heated sample (heating beam on), and (iii) a sample through the ablated areas (to cross-check the spatial overlap between the pump and probe).

Throughout the experiment, a typical XANES spectrum is obtained after the accumulation of ∼300 shots. The corresponding noise level achieved is 4%–5% rms, limited by the photon-counting statistics on the transmission spectrometer. In Fig. 2, we report a XANES spectrum recorded through samples at ambient temperature after an accumulation of 9256 shots (labeled "cold spectrum" in the following). Absorption is set to zero below the $L3$ edge and normalized above the $L2$ edge. The noise level estimated from the detected photon statistics lies below 1%. Excellent agreement is found with the *ab initio*

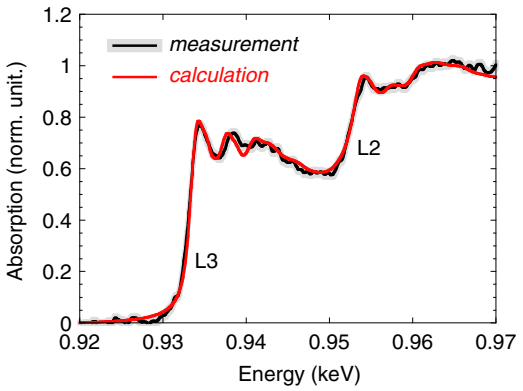

FIG. 2. Experimental and calculated XANES spectra near the copper L edge in ambient conditions. The experimental spectrum is accumulated over 9256 shots. The estimated noise level is reported in the shaded area.

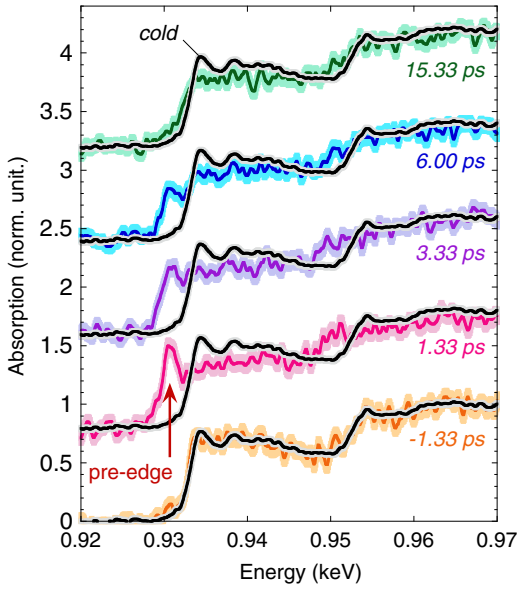

FIG. 3. Some time-resolved XANES spectra at an incident fluence of 1.4 ± 0.3 J/cm^2. Absorption spectra were artificially vertically shifted and superimposed with the cold spectrum. Delays between pump and probe pulses are indicated next to each spectrum.

XANES spectrum calculated in the same ambient conditions (see details below).

III. TIME-RESOLVED MEASUREMENTS

A. XANES spectra

Some time-resolved XANES spectra are shown in Fig. 3, corresponding to different delays of the x-ray probe relative to the laser pump with an incident fluence of 1.4 ± 0.3 J/cm^2. For negative delays, i.e., before the heating, spectra were superimposed on the cold one that was plotted for comparison. Just after the heating, pre-edge structures were observed a few eV below the $L3$ and $L2$ edges. These structures reached their maximum values right after heating. Then they gradually decreased on an ~10-ps time scale, in good general agreement with the observations reported by Cho *et al.* [12]. Such measurements were performed for a wide range of delays (up to ~30 ps) and incident fluence values (up to a few J/cm^2), each time leading to this same general observation.

B. Electron temperature retrieval

The pre-edge structures are intimately connected to the electron temperature [12]. Indeed, the x-ray photon absorption process provokes the transition of an electron from a bound state ($2p^{3/2}$ and $2p^{1/2}$ for the Cu $L3$ and $L2$ edges, respectively) to an available state near the continuum that satisfies the dipole selection rule (thus the $4s$ or $3d$ state). In that sense, XANES spectroscopy is representative of the unoccupied electron DOS. In ambient conditions, the $3d$ band is filled and located a few eV below the Fermi energy E_F that contributes to the absorption edges, being the frontier between occupied and unoccupied states. When increasing the electron temperature T_e, some electrons leave the $3d$ band to explore higher-energy states. The induced $3d$ unoccupied states allow new transitions

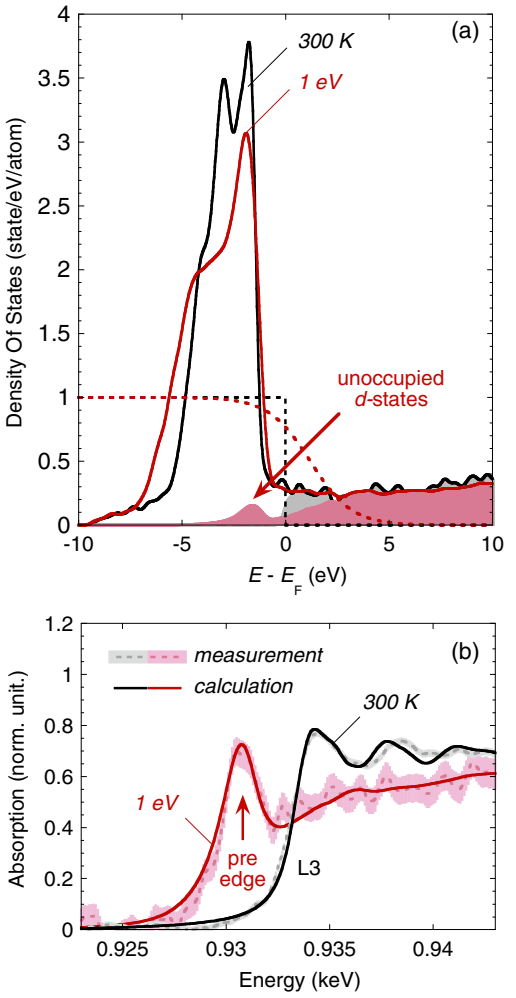

FIG. 4. (a) Copper electron DOS for the cold (solid state at 300 K) and 1 eV (liquid-state) samples. Fermi-Dirac distributions at these temperatures are represented by the dotted lines. The shaded areas represent the unoccupied DOS. (b) Corresponding calculated XANES spectra. The experimental spectra are taken, respectively, from the cold one in Fig. 2 and 1.33 ps after the heating in Fig. 3.

and lead to an absorption pre-edge a few eV below the L edge. The same considerations apply for both edges but are less visible at the $L2$ edge that presents a weaker magnitude [30].

To go further, *ab initio* quantum molecular dynamics (QMD) simulations have been performed. The general description of such calculations can be found in Ref. [25] and references therein. Simulations of warm dense copper will be the subject of a future publication. Nonequilibrium situations are generated by independent control of the electron and ion temperatures T_e and T_i. These two-temperature simulations have already been successful at predicting the behavior of metals irradiated by ultrashort lasers [31–33]. Different densities ρ are also considered to estimate the effect of possible sample expansion on the electronic structure and the resulting XANES spectra.

The effect of the rise in T_e is illustrated in Fig. 4. The DOS is dominated by the $3d$ band, completely filled at 300 K. In the liquid phase at 1 eV, the DOS is slightly changed, but the main modification in the unoccupied DOS (a bump of a few eV below

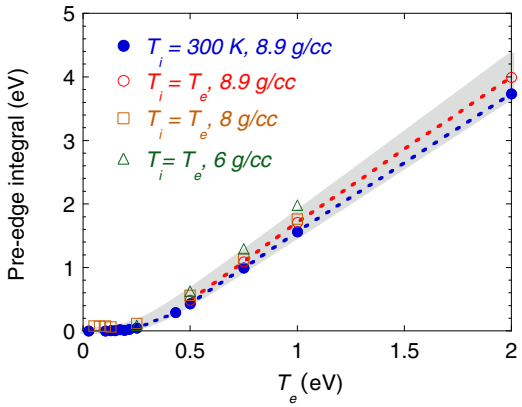

FIG. 5. Relation between the spectral integration of the pre-edge and T_e for different calculations in the nonequilibrium solid state ($T_i = 300$ K and ρ_{solid}) and at thermal equilibrium ($T_e = T_i$) at solid density ($\rho_{\text{solid}} = 8.9\,\text{g/cm}^3$), at liquid density ($\rho_{\text{liquid}} = 8\,\text{g/cm}^3$), and in an expanded liquid ($\rho = 6\,\text{g/cm}^3$).

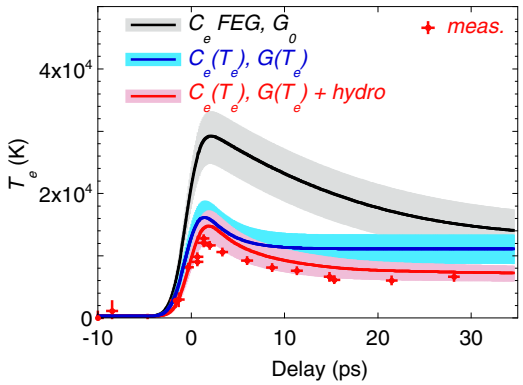

FIG. 6. Temporal evolution of T_e deduced from time-resolved spectra at incident fluence of $1.4 \pm 0.3\,\text{J/cm}^2$ (red crosses). The lines result from TTM calculations using different sets of coefficients. The last one (in red) takes into account the hydrodynamic expansion. Calculations are convoluted with the time response function of the measurements. Fluence uncertainty is reported in the shaded areas.

E_F) comes from the T_e-induced broadening of the Fermi-Dirac distribution. The calculation of the x-ray absorption probability is not *a priori* reduced to this single electron DOS since it integrates the phase of the photoelectron wave function and its scattering on the nearest-neighbor atoms [34]. However, the calculated XANES spectrum clearly emphasizes the correlation between the pre-edge and the bump mentioned above in the unoccupied DOS. Note the excellent agreement with the measurement reported in Fig. 4.

Calculations are performed under different thermodynamic conditions (ρ, T_e, T_i) and states (solid and liquid). The pre-edge features are obtained by spectral integration up to 0.9333 keV of the subtraction of heated spectra from the cold spectrum. The results are plotted in Fig. 5 as a function of T_e. Below ~0.25 eV, the pre-edge does not emerge significantly from the cold $L3$ edge. Beyond this value, the relation is roughly linear in the investigated range (several eV). The most interesting observation is the low effect of ρ, T_i, and phase (highlighted by the shaded area). That guarantees the unambiguous determination of T_e in all the conditions we have explored.

C. Electron temperature dynamics

Based on the above analysis, the temporal evolution of T_e is retrieved from the experimental TR-XANES spectra. The results concerning the incident fluence of $1.4 \pm 0.3\,\text{J/cm}^2$ (the same as in Fig. 3) are shown in Fig. 6. Measurements are compared with different calculations that will be discussed further. Experimental error bars integrate the slight dependence on ρ and T_i observed in Fig. 5. T_e reaches its maximum value right after heating, then decreases in about 10 ps, tending toward a more stable value at longer times. Such behavior is expected in the TTM [26]: the laser pulse quickly deposits its energy in the electrons before they progressively equilibrate with the ions.

The T_e rise time is expected to lie within a few hundred femtoseconds, resulting both from the heating laser pulse duration (300-fs FWHM) and the time needed to homogenize the sample thickness (~100 fs) [8,35,36]. The measurements give a larger value, from which the temporal resolution of the experimental setup has been estimated to be 1.2 ± 0.2 ps rms. The latter is essentially limited by the x-ray pulse duration in the sample plane.

It is short enough to reveal nonequilibrium situations where $T_e > T_i$ in the first 10 ps following the fast heating. The T_e decrease reflects the electron-ion thermal equilibration dynamics.

IV. CALCULATIONS AND DISCUSSION

A. TTM without spatial dimension

The first approach generally proposed in the literature assumes a constant density and neglects any hydrodynamic aspects. In the TTM framework, such a problem without spatial dimension comes down to the following two equations driving the evolution of electron and ion temperatures T_e and T_i:

$$C_e \frac{dT_e}{dt} = -G(T_e - T_i) + S(t),$$
$$C_i \frac{dT_i}{dt} = G(T_e - T_i).$$

$S(t)$ is the source term that is fixed to a 300-fs FWHM Gaussian shape as the pump beam of the experiment. The remaining input parameter is the fluence absorbed in the sample. Such a quantity could be determined by solving the Helmholtz equation, as proposed in the ESTHER code, which will be described further. However, it is sensitive to some aspects difficult to control, the main one being the sample surface quality. Therefore, we prefer to perform dedicated *in situ* measurements.

Three calorimeters have been used to measure the incident (through a calibrated beam splitter), reflected, and transmitted energies, respectively. Results are presented in Fig. 7 as a function of the incident fluence up to $\sim 1\,\text{J/cm}^2$. The laser absorption starts from $11\% \pm 2\%$ at the lowest fluences, then progressively increases. For an incident fluence of $1.4\,\text{J/cm}^2$, corresponding to the data presented in Fig. 6, the exponential extrapolation leads to an absorption of $28\% \pm 3\%$ and thus to

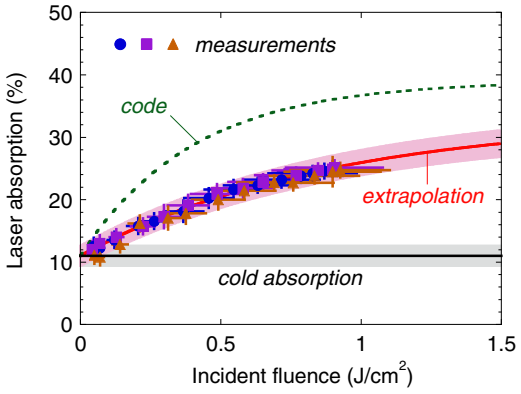

FIG. 7. Laser absorption measurements in the copper sample for different incident fluences, including values well below the damage threshold (labeled "cold absorption"). Values estimated by solving the Helmholtz equation are also indicated by the green dotted line.

an absorbed fluence of 0.4 ± 0.1 J/cm^2. This value is overestimated by the Helmholtz solver ($37\% \pm 1\%$). All subsequent calculations are performed using the measured values of laser absorption.

Different values are proposed in the literature for C_e, C_i, and G. The main ones are reported in Fig. 8 and come from Lin *et al.* [27]. At low temperature, a constant value of $G_0 = 10^{17}$ W m^{-3} K^{-1} is considered from published measurements [37]. C_e is linear with T_e as a result of the FEG model, and the slope is 96.8 J m^{-3} K^{-2} [38]. C_i is set to the value of the ambient solid, $C_i = 3.39 \times 10^6$ J m^{-3} K^{-1}. Such parameters lead to satisfactory agreement with previous optical experiments [35]. As can be observed in Fig. 6 (top black curve), our data show a clear disagreement with such "cold" assumptions. The maximum temperature measured is lower, revealing that a larger value should be considered for C_e, and the equilibration is faster, indicating that G is underestimated.

In the temperature range of several eV considered here (a few tens of thousands of kelvins), Lin *et al.* proposed the temperature-dependent parameters $C_e(T_e)$ and $G(T_e)$ plotted in Fig. 8 [27]. The resulting T_e temporal evolution is plotted in Fig. 6 (middle blue curve). As previously reported by Cho

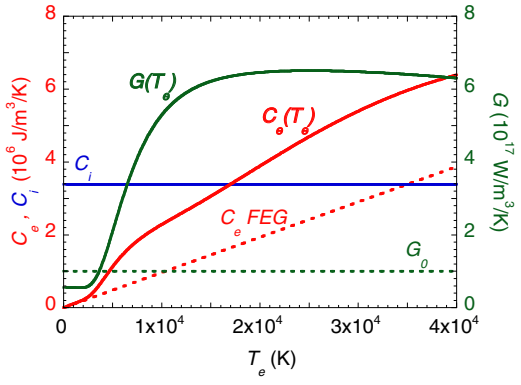

FIG. 8. Coefficients used for the TTM calculations. Dotted lines correspond to measured values at very low laser intensities, and a linear dependency with T_e is assumed for C_e in the FEG model. Thick solid lines are the T_e-dependent coefficients deduced by Lin *et al.* [27].

et al., the agreement was more satisfactory [12], especially regarding the maximum temperature achieved. Nevertheless, the calculation still overestimated $T_e(t)$ at long delays.

B. Two-temperature hydrodynamic calculations

In order to refine the description of the sample evolution after heating, we finally consider the transport and hydrodynamic motion with the one-dimensional hydrodynamic code ESTHER in which the TTM is consistently integrated [39]. The matter evolution is described with multiphase Bushman Lomonosov Fortov (BLF) equations of state [40] and consistent ion heat capacity C_i, so that C_i depends on both ionic temperature and density. $C_e(T_e)$ and $G(T_e)$ are taken from Lin *et al.* [27] with a density dependence in order to describe expanded matter. The laser absorption could be calculated by solving the Helmholtz equations, but we force the absorbed fluence to the measured value (see Fig. 7).

Another important ingredient in the code concerns the longitudinal energy transport through the sample thickness. Probing a sample with a temperature gradient could affect the validity of the T_e retrieval. The latter results from the comparison between the experimental XANES spectrum (longitudinally averaged) and the *ab initio* calculation (single cell with defined temperatures). The laser pulse deposits its energy in the skin depth (∼15 nm in copper); then homogenization is ensured by energy transport. Temperature-dependent data have been tabulated for the thermal conductivity in metals, leading to lower than 1000 W m^{-1} K^{-1} in the range of interest [41]. Such values lead to the relatively long time (∼10 ps) for temperature homogenization over the 80-nm copper thickness. More recent experimental studies have demonstrated that the ballistic electrons could rapidly homogenize the heating of a gold sample over ∼100 nm [35]. But this value could be reduced by a factor of 3 for absorbed fluence >200 mJ/cm^2 [36].

The effect of any residual temperature gradient on the T_e retrieval from XANES measurement has been numerically checked. On the one hand, the x-ray absorption through the sample is intrinsically the longitudinal integration of the photoabsorption cross section. On the other hand, the relation between the pre-edge and T_e is essentially linear. As a consequence, in the range of temperature considered here (typically, from ∼2000 up to ∼20 000 K), we have checked that the value of T_e retrieved from the pre-edge remains very close to the average value of T_e over the sample thickness (within a few percent, i.e., below the experimental error bars).

C. Simulation results

The temporal evolution of T_e resulting from the two-temperature hydrodynamic calculations described above is plotted in Fig. 6 (bottom red curve). The agreement with experimental data is excellent, not only at the shortest times (as already observed without hydrodynamics) but also for the long delays (⩾10 ps). Two entangled effects contribute to the modification in T_e dynamics. The density decreases during the sample hydrodynamic expansion, leading to an associated change in the TTM parameters values (C_i, C_e, and G). Meanwhile, some of the deposited energy is converted into kinetic energy.

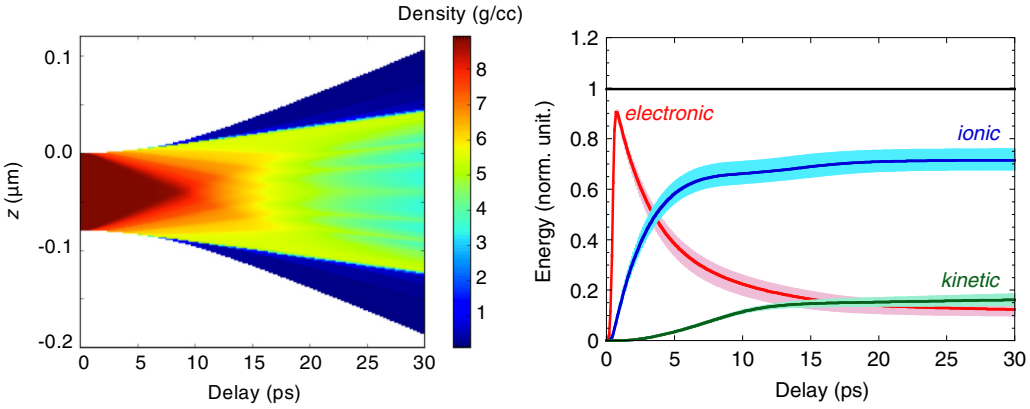

FIG. 9. Results of two-temperature hydrodynamic calculations performed for an 80-nm copper foil in which 0.4 ± 0.1 J/cm^2 is uniformly deposited in 300-fs FWHM (same conditions as in Fig. 6). Left: Two-dimension (longitudinal/temporal) evolution of the density indicated (in g/cm^3) by the color scale. Right: Corresponding temporal evolution of the energy balance.

Some simulation outputs are presented in Fig. 9, with the same absorbed fluence as in Fig. 6. On the left, the density map highlights the significant sample expansion in the first 10 ps. Initiated by the kinetic pressure, two ablation fronts start from both sides and propagate inward in the sample with the sound velocity (estimated as $c_s \sim 5$ km/s from the BLF equations of state). They join in the middle of the copper foil (thickness d) in $\tau_{\text{exp}} = d/2c_s \sim 8$ ps, i.e., in a time scale comparable to the electron-ion thermal equilibration. The average density continues to decrease down to $\sim$4 g/cm^3 at 30 ps. On the right, the energy balance is plotted. The laser is first deposited in the electron thermal energy, then progressively transferred to ion thermal energy. A significant part is also converted into kinetic energy that reaches about 15% at long delays.

Simulations have been performed while keeping the same absorbed fluence but considering the other layers of the sample: the plastic substrate and 10-nm a-C layer on the laser side. In a range of a few tens of picoseconds, the hydrodynamic expansion is not severely modified, essentially because of the low density of these layers compared to copper. Indeed, measurements have been performed on samples without the a-C layer without any significant difference being observed in XANES spectra. When considering thicker and denser layers (100-nm silicon), simulations show partial density confinement, but significant energy ($\sim$10%) is still converted into kinetic energy to set the Si layers in motion. As expected, this conversion ratio increases with the absorbed fluence.

Measurements have been performed for different incident fluences. Results are plotted in Fig. 10. They are compared with the two-temperature hydrodynamic simulations described above. No free parameter is introduced in calculations as the absorbed fluences are set to the measured value (see Fig. 7). Good agreement is observed both in amplitude and in the equilibration dynamics. For the lowest fluence (0.04 ± 0.01 J/cm^2 absorbed), the impact of the hydrodynamic expansion in the calculated $T_e(t)$ goes below the experimental error bars.

D. Discussion

Experimental data are well reproduced by two temperature simulations based on the parameters calculated from Lin *et al.*, with the condition of taking into account the hydrodynamic expansion of the heated foil. A more ambitious goal would be to infer parameter values directly from the experiment. This is *a priori* complex because the respective effects of C_i, C_e, and G are entangled in the observables and even more so because they depend on temperature and density.

When considering the simplified TTM model with constant parameters, one can analytically solve the equations presented in Sec. IV A and find an exponential behavior for the thermal equilibration between electrons and ions. The value of C_e can then be simply deduced from the ratio between absorbed fluence and T_e [16]. In a more realistic situation, it is necessary to be attentive to the strong temperature dependence of C_e during the fast heating. In contrast, the hydrodynamic expansion should not have a significant impact on such C_e determination since the corresponding time scale ($\sim$10 ps) is large compared to the heating (300-fs FWHM). This is unfortunately no longer the case when considering the observed values of equilibrated temperature and equilibration characteristic time for possible determination of C_i and G.

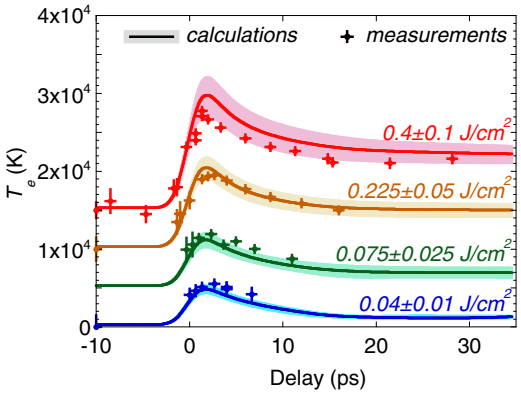

FIG. 10. Evolution of T_e as retrieved from measurements at different heating fluences and comparison with two-temperature hydrodynamic calculations. The indicated values refer to the absorbed fluence estimated from the laser absorption measurements. The plots are artificially vertically shifted. Calculations are convoluted with the temporal resolution of the experiment.

We can trust the ion heat capacity values estimated from the BLF equation of state since it has been built from experimental data in a wide range of density-temperature conditions [40]. In Lin *et al.*, the electron heat capacity is directly calculated from the solid-state electron DOS. In the range of densities and temperatures under consideration here, *ab initio* QMD simulations show that such a DOS is not modified enough (see, e.g., Fig. 4) to significantly affect the value of $C_e(T_e)$. The discussion is more open concerning the electron-ion coupling factor G since the calculation of Lin *et al.* assumes a solid-state DOS for both electrons and phonons. We can thus expect a strong disagreement once the lattice has disappeared above melting.

The value of G is encoded in the characteristic time of the T_e decrease down to equilibration but with the cross influence of C_e, C_i, and hydrodynamic expansion. In order to find a value for G from the experimental data, we have considered the full two-temperature hydrodynamic simulations described above, but assuming a value of G independent of T_e. The density dependence is kept. Considering the experimental error bars, we find satisfactory agreement with $G = 6 \pm 2 \times 10^{17}$ W m^{-3} K^{-1}. That fits well with the predicted value in the corresponding T_e range from 10 000 to 20 000 K (see Fig. 8 and Ref. [27]).

V. CONCLUSION

In conclusion, we have performed time-resolved XANES measurements with a tabletop setup to investigate nonequilibrium warm dense copper produced by a femtosecond optical laser pulse. The electron temperature is retrieved from a pre-edge structure observed near the L edge, thanks to careful *ab initio* simulations. The picosecond dynamics of the electron-ion thermal equilibration is well reproduced by two-temperature model calculations only when the temperature and density dependence of electron and ion heat capacities and electron-ion coupling are considered. In the temperature range investigated (up to ∼20 000 K), the hydrodynamic expansion induced by the high pressure achieved cannot be ignored and affects significantly the energy balance between electrons and ions. Even if the investigated conditions are far from the solid-state assumptions of Lin *et al.*, satisfactory agreement is found with the temperature-dependent electron-ion coupling factor that they proposed.

ACKNOWLEDGMENTS

This work was supported by the French Agence Nationale de la Recherche, under Grant No. OEDYP (ANR-09-BLAN-0206-01), and the Conseil Régional d'Aquitaine, under Grant No. POLUX (2010-13-04-002). The authors gratefully acknowledge A. Filippov, R. Bouillaud, and L. Merzeau for their technical assistance and F. Burgy and C. Pégeot for laser operation. They also thank M. Millerious from CEA and M. Störmer from Helmholtz Zentrum Geesthacht for the sample realization. The authors thank M. Torrent for his great help with ABINIT simulations.

[1] National Research Council, *Frontiers in High Energy Density Physics: The X-Games of Contemporary Science* (National Academies Press, Washington, DC, 2003).
[2] M. Ross, Nature (London) **292**, 435 (1981).
[3] T. Guillot, Science **286**, 72 (1999).
[4] A. Benuzzi-Mounaix, S. Mazevet, A. Ravasio, T. Vinci, A. Denoeud, M. Koenig, N. Amadou, E. Brambrink, F. Festa, A. Lévy, M. Harmand, S. Brygoo, G. Huser, V. Recoules, J. Bouchet, G. Morard, F. Guyot, T. de Resseguier, K. Myanishi, N. Ozaki, F. Dorchies, J. Gaudin, P. M. Leguay, O. Peyrusse, O. Henry, D. Raffestin, S. Le Pape, R. Smith, and R. Musella, Phys. Scr. T **161**, 014060 (2014).
[5] M. Koenig, A. Benuzzi, B. Faral, J. Krishnan, J. M. Boudenne, T. Jalinaud, C. Rémond, A. Decoster, D. Batani, D. Beretta, and T. A. Hall, Appl. Phys. Lett. **72**, 1033 (1998).
[6] T. Plisson, P. Colin-Lalu, G. Huser, and P. Loubeyre, J. Appl. Phys. **120**, 085903 (2016).
[7] J. W. Chan, T. Huser, S. Risbud, and D. M. Krol, Opt. Lett. **26**, 1726 (2001).
[8] K. Widmann, T. Ao, M. E. Foord, D. F. Price, A. D. Ellis, P. T. Springer, and A. Ng, Phys. Rev. Lett. **92**, 125002 (2004).
[9] T. Ao, Y. Ping, K. Widmann, D. F. Price, E. Lee, H. Tam, P. T. Springer, and A. Ng, Phys. Rev. Lett. **96**, 055001 (2006).
[10] Y. Ping, D. Hanson, I. Koslow, T. Ogitsu, D. Prendergast, E. Schwegler, G. Collins, and A. Ng, Phys. Rev. Lett. **96**, 255003 (2006).
[11] R. Ernstorfer, M. Harb, C. T. Hebeisen, G. Sciaini, T. Dartigalongue, and R. J. Dwayne Miller, Science **323**, 1033 (2009).
[12] B. I. Cho, K. Engelhorn, A. A. Correa, T. Ogitsu, C. P. Weber, H. J. Lee, J. Feng, P. A. Ni, Y. Ping, A. J. Nelson, D. Prendergast, R. W. Lee, R. W. Falcone, and P. A. Heimann, Phys. Rev. Lett. **106**, 167601 (2011).
[13] F. Dorchies, A. Lévy, C. Goyon, P. Combis, D. Descamps, C. Fourment, M. Harmand, S. Hulin, P. M. Leguay, S. Petit, O. Peyrusse, and J. J. Santos, Phys. Rev. Lett. **107**, 245006 (2011).
[14] Z. Chen, B. Holst, S. E. Kirkwood, V. Sametoglu, M. Reid, Y. Y. Tsui, V. Recoules, and A. Ng, Phys. Rev. Lett. **110**, 135001 (2013).
[15] P. M. Leguay, A. Lévy, B. Chimier, F. Deneuville, D. Descamps, C. Fourment, C. Goyon, S. Hulin, S. Petit, O. Peyrusse, J. J. Santos, P. Combis, B. Holst, V. Recoules, P. Renaudin, L. Videau, and F. Dorchies, Phys. Rev. Lett. **111**, 245004 (2013).
[16] B. I. Cho, T. Ogitsu, K. Engelhorn, A. A. Correa, Y. Ping, J. W. Lee, L. J. Bae, D. Prendergast, R. W. Falcone, and P. A. Heimann, Sci. Rep. **6**, 18843 (2016).
[17] U. Zastrau, C. Fortmann, R. R. Faüstlin, L. F. Cao, T. Döppner, S. Düsterer, S. H. Glenzer, G. Gregori, T. Laarmann, H. J. Lee, A. Przystawik, P. Radcliffe, H. Reinholz, G. Röpke, R. Thiele, J. Tiggesbäumker, N. X. Truong, S. Toleikis, I. Uschmann, A. Wierling, T. Tschentscher, E. Förster, and R. Redmer, Phys. Rev. E **78**, 066406 (2008).
[18] R. R. Faüstlin, Th. Bornath, T. Döppner, S. Düsterer, E. Förster, C. Fortmann, S. H. Glenzer, S. Göde, G. Gregori, R. Irsig, T. Laarmann, H. J. Lee, B. Li, K.-H. Meiwes-Broer, J. Mithen, B. Nagler, A. Przystawik, H. Redlin, R. Redmer, H. Reinholz, G. Röpke, F. Tavella, R. Thiele, J. Tiggesbäumker, S. Toleikis, I. Uschmann, S. M. Vinko, T. Whitcher, U. Zastrau, B. Ziaja, and Th. Tschentscher, Phys. Rev. Lett. **104**, 125002 (2010).
[19] O. Ciricosta, S. M. Vinko, H.-K. Chung, B. I. Cho, C. R. D. Brown, T. Burian, J. Chalupský, K. Engelhorn, R. W. Falcone, C.

Graves, V. Hájková, A. Higginbotham, L. Juha, J. Krzywinski, H. J. Lee, M. Messerschmidt, C. D. Murphy, Y. Ping, D. S. Rackstraw, A. Scherz, W. Schlotter, S. Toleikis, J. J. Turner, L. Vysin, T. Wang, B. Wu, U. Zastrau, D. Zhu, R. W. Lee, P. A. Heimann, B. Nagler, and J. S. Wark, Phys. Rev. Lett. **109**, 065002 (2012).

[20] S. M. Vinko, O. Ciricosta, B. I. Cho, K. Engelhorn, H.-K. Chung, C. R. D. Brown, T. Burian, J. Chalupský, R. W. Falcone, C. Graves, V. Hájková, A. Higginbotham, L. Juha, J. Krzywinski, H. J. Lee, M. Messerschmidt, C. D. Murphy, Y. Ping, A. Scherz, W. Schlotter, S. Toleikis, J. J. Turner, L. Vysin, T. Wang, B. Wu, U. Zastrau, D. Zhu, R. W. Lee, P. A. Heimann, B. Nagler, and J. S. Wark, Nature (London) **482**, 59 (2012).

[21] G. M. Dyer, A. C. Bernstein, B. I. Cho, J. Osterholz, W. Grigsby, A. Dalton, R. Shepherd, Y. Ping, H. Chen, K. Widmann, and T. Ditmire, Phys. Rev. Lett. **101**, 015002 (2008).

[22] A. Mancic, A. Lévy, M. Harmand, M. Nakatsutsumi, P. Antici, P. Audebert, P. Combis, S. Fourmaux, S. Mazevet, O. Peyrusse, V. Recoules, P. Renaudin, J. Robiche, F. Dorchies, and J. Fuchs, Phys. Rev. Lett. **104**, 035002 (2010).

[23] A. Rousse, C. Rischel, S. Fourmaux, I. Uschmann, S. Sebban, G. Grillon, Ph. Balcou, E. Förster, J. P. Geindre, P. Audebert, J. C. Gauthier, and D. Hulin, Nature (London) **410**, 65 (2001).

[24] B. J. Siwick, J. R. Dwyer, R. E. Jordan, and R. J. D. Miller, Science **302**, 1382 (2003).

[25] F. Dorchies and V. Recoules, Phys. Rep. **657**, 1 (2016).

[26] S. I. Anisimov, B. L. Kapeliovich, and T. L. Perel'man, Sov. Phys. JETP **39**, 375 (1974).

[27] Z. Lin, L. V. Zhigilei, and V. Celli, Phys. Rev. B **77**, 075133 (2008).

[28] F. Dorchies, N. Fedorov, and L. Lecherbourg, Rev. Sci. Instrum. **86**, 073106 (2015).

[29] A. Lévy, F. Dorchies, C. Fourment, M. Harmand, S. Hulin, J. J. Santos, D. Descamps, S. Petit, and R. Bouillaud, Rev. Sci. Instrum. **81**, 063107 (2010).

[30] H. Ebert, J. Stöhr, S. S. P. Parkin, M. Samant, and A. Nilsson, Phys. Rev. B **53**, 16067 (1996).

[31] B. Holst, V. Recoules, S. Mazevet, M. Torrent, A. Ng, Z. Chen, S. E. Kirkwood, V. Sametoglu, M. Reid, and Y. Y. Tsui, Phys. Rev. B **90**, 035121 (2014).

[32] D. V. Knyazev and P. R. Levashov, Phys. Plasmas **21**, 073302 (2014).

[33] S. Mazevet, J. Clerouin, V. Recoules, P. M. Anglade, and G. Zerah, Phys. Rev. Lett. **95**, 085002 (2005).

[34] *X-ray Absorption: Principles, Applications, Techniques of EXAFS, SEXAFS, XANES*, edited by D. C. Koningsberger and R. Prins (Wiley, New York, 1988).

[35] J. Hohlfeld, S. S. Wellershoff, J. Güdde, U. Conrad, V. Jähnke, and E. Matthias, Chem. Phys. **251**, 237 (2000).

[36] T. Ogitsu, Y. Ping, A. Correa, B. I. Cho, P. Heimann, E. Schwegler, J. Cao, and G. W. Collins, High Energy Density Phys. **8**, 303 (2012).

[37] H. E. Elsayed-Ali, T. B. Norris, M. A. Pessot, and G. A. Mourou, Phys. Rev. Lett. **58**, 1212 (1987).

[38] *American Institute of Physics Handbook*, 3rd ed. (McGraw-Hill, New York, 1972).

[39] J.-P. Colombier, P. Combis, F. Bonneau, R. Le Harzic, and E. Audouard, Phys. Rev. B **71**, 165406 (2005).

[40] A. V. Bushman, I. V. Lomonosov, and V. E. Fortov, Sov. Technol. Rev., Ser. B **5**, 1 (1993).

[41] Y. S. Touloukian, R. W. Powell, C. Y. Ho, and P. G. Klemens, in *Thermophysical Properties of Matter: The TPRC Data Series*, Thermal Conductivity–Metallic Elements and Alloys (Plenum Press, New York, 1970), Vol. 1, 1595 pp.